ACS APPLIED MATERIALS & INTERFACES

Research Article

www.acsami.org

Hydrogenated Oxygen-Deficient Blue Anatase as Anode for High-Performance Lithium Batteries

Jing Zheng,[†] Yousong Liu,[†] Guangbin Ji,*[,†] Peng Zhang,[‡] Xingzhong Cao,[‡] Baoyi Wang,[‡] Chuhong Zhang,*[,§] Xuguang Zhou,[∥] Yan Zhu,[∥] and Daning Shi[∥]

[†]College of Materials Science and Technology, Nanjing University of Aeronautics and Astronautics, Nanjing 210016, P. R. China

[‡]Key Laboratory of Nuclear Analysis Techniques, Institute of High Energy Physics, Chinese Academy of Sciences, Beijing 100049, P. R. China

[§]State Key Lab of Polymer Materials Engineering, Polymer Research Institute, Sichuan University, Chengdu 610065, P. R. China

[∥]College of Science, Nanjing University of Aeronautics and Astronautics, Nanjing 211100, P. R. China

Supporting Information

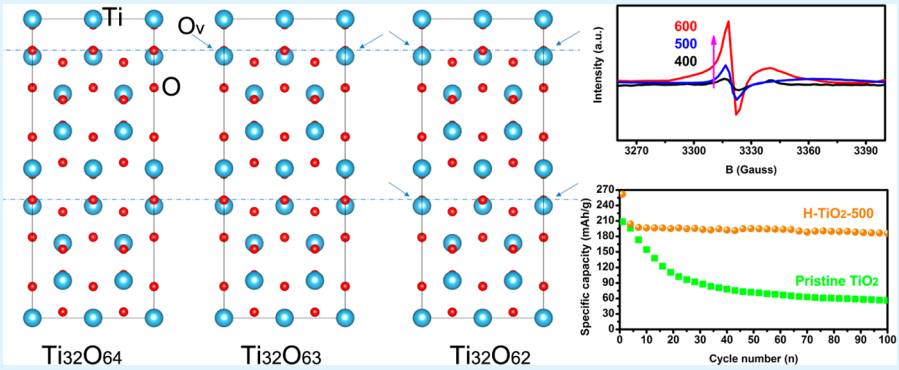

ABSTRACT: Blue oxygen-deficient nanoparticles of anatase TiO_2 (H-TiO_2) are synthesized using a modified hydrogenation process. Scanning electron microscope and transmission electron microscope images clearly demonstrate the evident change of the TiO_2 morphology, from 60 nm rectangular nanosheets to much smaller round or oval nanoparticles of ~17 nm, after this hydrogenation treatment. Importantly, electron paramagnetic resonance and positronium annihilation lifetime spectroscopy confirm that plentiful oxygen vacancies accompanied by Ti^{3+} are created in the hydrogenated samples with a controllable concentration by altering hydrogenation temperature. Experiments and theory calculations demonstrate that the well-balanced Li^+/e^- transportation from a synergetic effect between Ti^{3+}/oxygen vacancy and reduced size promises the optimal H-TiO_2 sample a high specific capacity, as well as greatly enhanced cycling stability and rate performance in comparison with the other TiO_2.

KEYWORDS: *anatase TiO_2, hydrogenation treatment, oxygen vacancy dependence, Li-storage performance, synergetic effect*

INTRODUCTION

Recently, titanium dioxide (TiO_2) has attracted great attention as anode materials in rechargeable lithium-ion batteries (LIBs) due to its potential advantages, such as low cost, nontoxicity, high stability, and excellent cyclability. However, the low lithium-ion mobility and the poor electronic conductivity prevent TiO_2 from practical application in LIBs.[1,2] Therefore, the development of simple and effective synthesis strategies for high-performance TiO_2 anode materials is much desired.

Design of nanostructured TiO_2 has been proved effective in shortening the Li^+ diffusion pathway, and the nanostructure (nanoparticles, nanowires, nanotubes, mesoporous materials, etc.) is critical to its electrochemical performance.[3−7] Coating or linking conductive components on/with TiO_2, such as sp^2-hybridizated carbon, is another common route to modify the surface electronic properties of TiO_2, which is complex and ineffective for large-scale production though.[8−11] People also establish techniques of doping TiO_2 with foreign elements, such as niobium,[12] tin,[13] and nitrogen,[14] to regulate the band gap for enhanced electronic conductivity. However, the conductivity is still hardly sufficient for practical application. Recently, hydrogenation treatment has been developed as a facile technique to create plentiful oxygen vacancies in TiO_2, which can remarkably boost its electronic conductivity.[15−17] Rather than only producing a thin conductive layer on the surface, this H_2 reduction method is able to turn the whole TiO_2 electrode to highly conductive semiconductor.[18] In addition, this novel strategy is simple and can directly remove

Received: May 5, 2015
Accepted: October 12, 2015
Published: October 12, 2015

DOI: 10.1021/acsami.5b07000
ACS Appl. Mater. Interfaces 2015, 7, 23431−23438

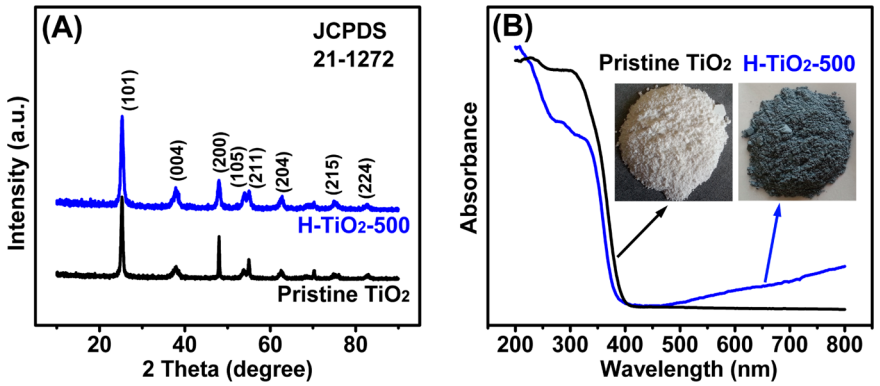

Figure 1. (A) X-ray diffraction patterns and (B) UV−vis reflectance spectra of the pristine TiO_2 and H-TiO_2-500.

the oxygen atoms from TiO_2 to generate oxygen vacancies, which avoids inactive Li-storage constituents that may hinder the Li^+ diffusion. However, these oxygen vacancies in TiO_2 generate a large number of defects, which in turn deplete the concentration of Li^+ charge carriers, thus slowing the Li^+ diffusion. Therefore, to control the concentration of the oxygen vacancies is the key factor for fast Li^+ diffusion as well as high electronic conductivity.[19,20]

Hydrogenation treatment conducted at different conditions, such as atmospheric hydrogen mixture (5% H_2+95% Ar, 1 atm, 450 °C), high-pressure pure hydrogen (H_2, 20 bar, 200 °C or H_2, 40 bar, 450 °C), etc., have been reported,[21,22] and the resulting materials exhibit various electrochemical properties. In this paper, we report a modified and relatively moderate hydrogenation process (pure H_2 under ca. 1 atm instead of under high-pressure environment), by which blue hydrogenated round anatase nanoparticles are obtained using rectangular anatase TiO_2 nanosheets as start materials. They are then used and tested as anode materials for LIBs. The effect of hydrogenation temperature on the structure defects and thus the electrochemical performance of the H-TiO_2 are investigated in detail. The electron paramagnetic resonance (EPR) results and the positron annihilation lifetime spectra (PALS) demonstrate that abundant oxygen vacancies and Ti^{3+} are successfully introduced by this hydrogenation process. The blue anatase TiO_2 hydrogenated at 500 °C possesses significantly higher energy capacity as well as better cyclability and rate performance than the white pristine TiO_2.

EXPERIMENTAL SECTION

Synthesis of Anatase TiO_2 Nanosheets. A modified hydrothermal route was employed to synthesize anatase TiO_2 nanosheets.[23] In a typical experiment, 25 mL of $Ti(OBu)_4$ (Sinopharm Chemical Reagent Co., Ltd.) and 3 mL of HF (35.35 wt% Nanjing Chemical Reagent Co., Ltd.) were mixed in a 100 mL dried Teflon-lined autoclave and maintained at 200 °C for 24 h. After being cooled to room temperature, TiO_2 nanosheets with average length of 60 nm were obtained by high-speed centrifugation and then were washed with distilled water and absolute ethanol three times. The as-obtained TiO_2 is referred to as pristine TiO_2.

Hydrogenaion Treatment of TiO_2 Nanoparticles. Hydrogenation treatment was performed in an electric tube furnace equipped with a quartz tube reactor. The as-prepared TiO_2 nanosheet (1.2 g) was put into the tube furnace under a flow of pure Ar (purity 99.999%, 100 sccm) for 30 min to remove air in the furnace. Subsequently, the as-pretreated sample was heated to the set temperature (400, 500, and 600 °C) under pure hydrogen (99.999%) at a rate of 5 °C/min. The flow rate was fixed to 50 sccm, and the temperature was maintained for 0.5 h before it was cooled to room temperature. These samples were referred to as H-TiO_2-T (T = hydrogenation temperature [°C]). In addition, an oxygen-vacancy-free TiO_2 sample (denoted as TiO_2-17 nm-R, R means remove the oxygen vacancy) with the same size as H-TiO_2-500 was also synthesized via second heat treatment of H-TiO_2-500 at 500 °C for 10 h under air to remove oxygen vacancy but keep its original structure.

Computational Method. In our theoretical calculations, TiO_2 lattice was modeled using a 2 × 2 × 2 supercell with a molecular formula of $Ti_{32}O_{64}$. Calculations were performed using the Vienna Ab−initio Simulation Package (VASP),[24] which employed a density functional theory (DFT)-based plane-wave method.[25] Exchange correlation effects were included using the Perdew−Burke−Ernzerhof (PBE).[26] The energy cutoff for the expansion of wave function was set to be 380 eV, which was tested to be enough for both total energy in the systems. For geometry relaxation, 4 × 4 × 2 Monkhorst−Pack K-points were adopted for the calculation. To correct the on-site electron correlation, DFT plus Hubbard model (DFT+U) was employed, with U = 4.0 eV based on our tests and early publications.[27] The atomic position was optimized through PBE calculations with a criterion that required the calculated forces less than 1×10^{-2} eV/Å.

Structural Characterization. The anatase TiO_2 nanosheets before and after hydrogenation treatment were extensively characterized by X-ray diffraction analysis (XRD, Bruker D8 Advance X-ray diffractometer using a Cu Kα X-ray source), field emission scanning electron microscopy (FESEM, HITACHI S4800), high-resolution transmission electron microscopy (HRTEM, JEOL JEM 2100F), X-ray photoelectron spectrometry (XPS, Thermo ESCALAB 250), Raman spectroscopy (Raman, JY HR800), UV−vis diffuse reflectance spectra (UV−vis, Shimadzu UV = 3600), electron paramagnetic resonance (EPR, Bruker EMX-10/12), and positron annihilation technique spectroscopy (PALS, slow positron beam at institute of high energy physics, resolution = 197 ps).

Electrochemical Measurement. To prepare working electrode, the as-prepared pristine TiO_2 or H-TiO_2 materials, conductive carbon black, and polyvinylidene difluoride (PVDF) were mixed at a weight ratio of 75:15:10 in appropriate amount of *N*-methylpyrrolidinone (NMP) to obtain homogeneous yogurtlike slurry. The slurry was coated onto a thin copper foil, followed by drying at 80 °C for 12 h under vacuum. Electrode discs (diameter = 12 mm) were punched from the Cu foil, on which the typical loading of active material was ~1.0 mg/cm^2. CR2032 coin cells were assembled in an Ar-filled glovebox using pure lithium metal foils as counter electrode, a polypropylene microporous film as separator, 1 M $LiPF_6$ dissolved in a mixture of ethylene carbonate (EC), and dimethyl carbonate (DMC) 1:1 (w/w) as electrolyte. Galvanostatic charge/discharge tests were performed with LAND CT-2001A instrument (Wuhan, PRC) at a voltage range of 1.0−3.0 V versus Li/Li^+ at room temperature (23 ± 0.5 °C). Cyclic voltammetry (CV) and electrochemical impedance spectroscopy (EIS) were performed on a CHI660D electrochemical workstation (CH Instrument, Shanghai, PRC).

DOI: 10.1021/acsami.5b07000
ACS Appl. Mater. Interfaces 2015, 7, 23431−23438

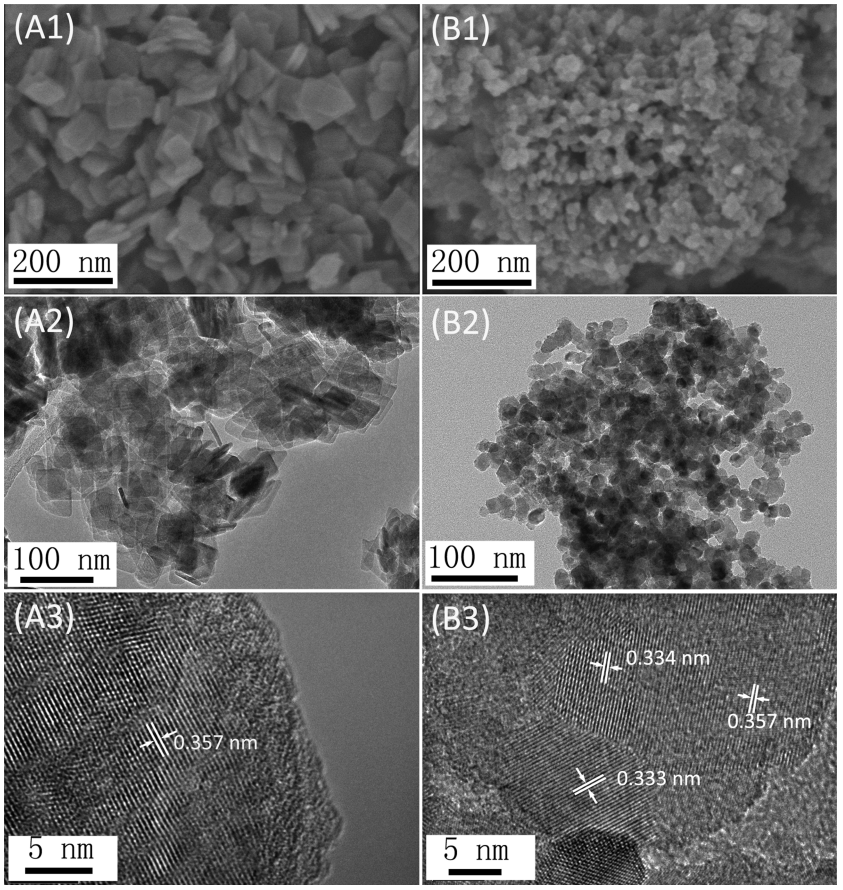

Figure 2. FESEM (A1, B1), TEM (A2, B2), and HRTEM (A3, B3) images of the (A) pristine TiO_2 and (B) H-TiO_2-500.

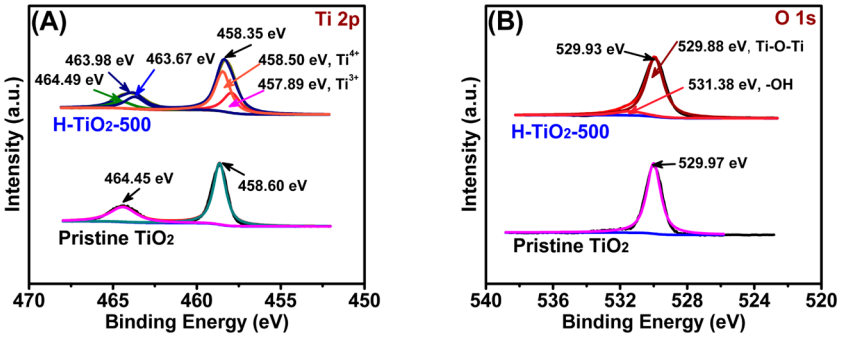

Figure 3. High-resolution XPS spectra of Ti 2p (A) and O 1s (B) of the pristine TiO_2 and H-TiO_2-500.

RESULTS AND DISCUSSION

Figure 1A shows the XRD patterns of pristine TiO_2 and H-TiO_2-500. Both samples exhibit typical diffraction peaks of anatase phase (JCPDS 21−1272) at 25.28°, 48.05°, 55.06°, 37.80°, 53.89°, and 62.69°, corresponding to the planes of (101), (200), (211), (004), (105), and (204), respectively. No other phases such as rutile TiO_2 or other reduced phases are observed, suggesting no obvious changes of the anatase framework after hydrogenation treatment. However, the color of TiO_2 is visually translated from white to blue, indicating that microstructure is changed to some extent, which further affects its optical properties. The UV−vis diffraction spectra of pristine TiO_2 and H-TiO_2-500 in Figure 1B show that they have similar signal response in UV region (200−400 nm), but a much larger absorption is observed on H-TiO_2-500 in the visible light range (400−800 nm). The optical changes of anatase TiO_2 after hydrogenation treatment could be attributed to the local Ti^{3+} centers (band at 620 nm) and oxygen vacancies (bands at 1060, 441, and 486 nm).[5,28]

The SEM and TEM images of pristine TiO_2 (Figure 2A1−A3) present uniform rectangular nanosheets with an average side length of ∼60 nm. After hydrogenation treatment, it can be obviously observed that these nanosheets were turned into round or oval nanoparticles with an average size of ∼17 nm (Figure 2B1−B3 and Figure S1). It indicates that the original thin nanosheet structure of TiO_2 is unstable under high-temperature hydrogen atmosphere, thus collapsing and reconstructing during the hydrogenation treatment. The resultant nanoparticles consist of many small grains with abundant grain boundaries. Furthermore, in addition to typical lattice fringes of (101) plane of anatase TiO_2 with a lattice distance of 0.357 nm, a new lattice fringe with a lattice distance

DOI: 10.1021/acsami.5b07000
ACS Appl. Mater. Interfaces 2015, 7, 23431−23438

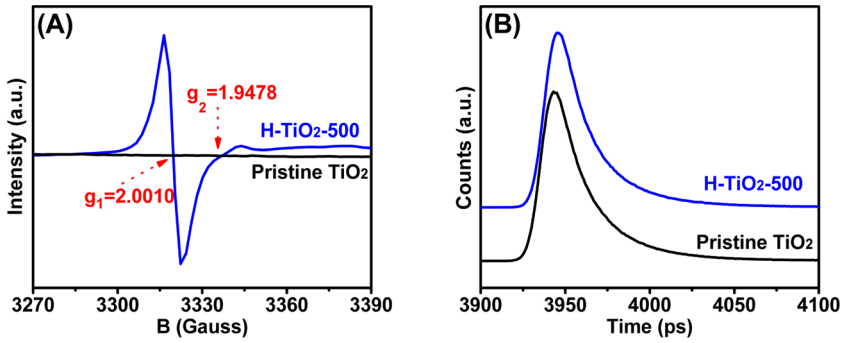

Figure 4. Low-temperature EPR (A) and PALS (B) spectra of pristine TiO_2 and H-TiO_2-500.

Table 1. Positron Lifetimes and Relative Intensities with Their Deviations for Pristine TiO_2 and H-TiO_2-T Samples at Different Temperature[a]

samples		τ_1 (ps)	τ_2 (ps)	τ_3 (ns)	I_1 (%)	I_2 (%)	I_3 (%)	I_1/I_2
pristine TiO_2	value	175.5	357.0	2.5820	46.10	49.30	4.66	0.94
	error	3.6	5.1	0.0240	1.40	1.40	0.14	
H-TiO_2-400	value	191.2	398.0	2.5950	60.80	34.80	4.40	1.75
	error	3.1	7.9	0.0270	1.30	1.30	0.13	
H-TiO_2-500	value	182.4	385.8	2.5740	63.30	32.00	4.69	1.98
	error	2.7	8.2	0.0330	1.30	1.30	0.13	
H-TiO_2-600	value	173.6	356.5	2.6210	52.00	43.50	4.43	1.19
	error	3.6	6.0	0.0320	1.40	1.40	0.14	

[a]T = 400, 500, 600 °C.

of 0.330 nm appears in H-TiO_2-500, corresponding to the (004) planes of Ti_6O_{11}. These results suggest that the hydrogenation process has made obvious deviation from the stoichiometry for TiO_2, possibly leading to the introduction of oxygen vacancies into TiO_2.

To deeply reveal the oxygen vacancy, multiple techniques, including XPS, EPR, and PALS, were employed to characterize the as-prepared samples. The original high-resolution Ti 2p XPS spectra in Figure S2 demonstrate that the full width at half-maximum (fwhm) for H-TiO_2-500 and pristine TiO_2 is 1.475 and 0.915 eV, respectively. Furthermore, a small shift of binding energy from 458.60 eV of pristine TiO_2 to 458.35 eV of H-TiO_2-500 is observed. Because these data are recorded on the same instrument under the same condition, we believe that these changes are probably attributed to the different chemical bonding environment of Ti 2p.[29,30] As shown in Figure 3A, after well deconvolution, a typical Ti^{4+} $2p_{3/2}$ signal peak at 458.60 and 458.50 eV for pristine TiO_2 and H-TiO_2-500 is observed, respectively. Importantly, an extra obvious signal at 457.89 eV is observed in H-TiO_2-500, corresponding to Ti^{3+} $2p_{3/2}$. In contrast, there is no obvious Ti^{3+} species observed in Ti 2p XPS spectrum of the pristine TiO_2. Similar results are found on the high-resolution O 1s XPS spectra shown in Figure 3B. Besides the similar signal peak of Ti−O−Ti bonds located at ∼529.9 eV for both samples, an extra peak centered at ∼531.38 eV is observed for H-TiO_2-500, which is attributed to Ti−OH species on the surface.[31] To some extent, these results of XPS analysis probably confirm that H_2 treatment has partially reduced Ti^{4+} to Ti^{3+} and created oxygen deficiencies.

To further identify the nature of radical species and the presence of oxygen vacancy/Ti^{3+} ions, low-temperature EPR spectra of the pristine TiO_2 and H-TiO_2-500 are recorded, as shown in Figure 4A. It has been reported that oxygen vacancy has a typical g-value of ∼2.004 and paramagnetic Ti^{3+} at g = 1.94−1.99.[32] Here, only the H_2-treated sample gives rise to very strong EPR signals, which can be fitted by two components with g = 2.0010 and 1.9478, corresponding to oxygen vacancy and Ti^{3+}, respectively. Moreover, the room-temperature EPR spectrum of H-TiO_2-500 shows smooth signals in the range of g = 1.94−1.99 of paramagnetic Ti^{3+}, as Ti^{3+} ions cannot be detected by EPR at room-temperature (Figure S3). The above results provide an effective proof for the existence of oxygen vacancy as well as Ti^{3+}.

Positron annihilation lifetime spectrum (PALS), which is useful at inquiring and determining vacancy-type defects in semiconductors, is employed here to provide information on the positron lifetimes and thus the concentration of vacancies.[33,34] Figure 4B illustrates typical positron PALS spectra of pristine TiO_2 and H-TiO_2-500. The positron lifetime is composed of three components, which can be evaluated by deconvolution of the positron decay spectrum D (t) using PATFIT program. The values of the three positron lifetime components, namely, τ_1, τ_2, and τ_3, and their corresponding intensities I_1, I_2, and I_3 are listed in Table 1. The first short lifetime of positrons τ_1 is generally due to the free annihilation of positrons in a defect-free crystal. However, some smaller vacancies and/or shallow positron traps in disordered crystals may reduce the surrounding electron density, leading to bigger values of τ_1. This might account for the fact that the τ_1 of H-TiO_2-500 (182.4 ps) is remarkably longer than that of pristine TiO_2 (175.5 ps). The longest lifetime component (τ_3) probably depends on the loading method of "sandwich" structure (i.e., the substrate material, the inevitable interface of specimen-positron and source-specimen), which has no useful information for revealing the defects of as-prepared TiO_2.

The intermediate lifetime component τ_2 is the most important one and can be attributed to positrons captured by the low electron density area or defects. The average electron density in larger-sized defects is lower than that in smaller defects, which decreases the annihilation rate and increases the

DOI: 10.1021/acsami.5b07000
ACS Appl. Mater. Interfaces 2015, 7, 23431−23438

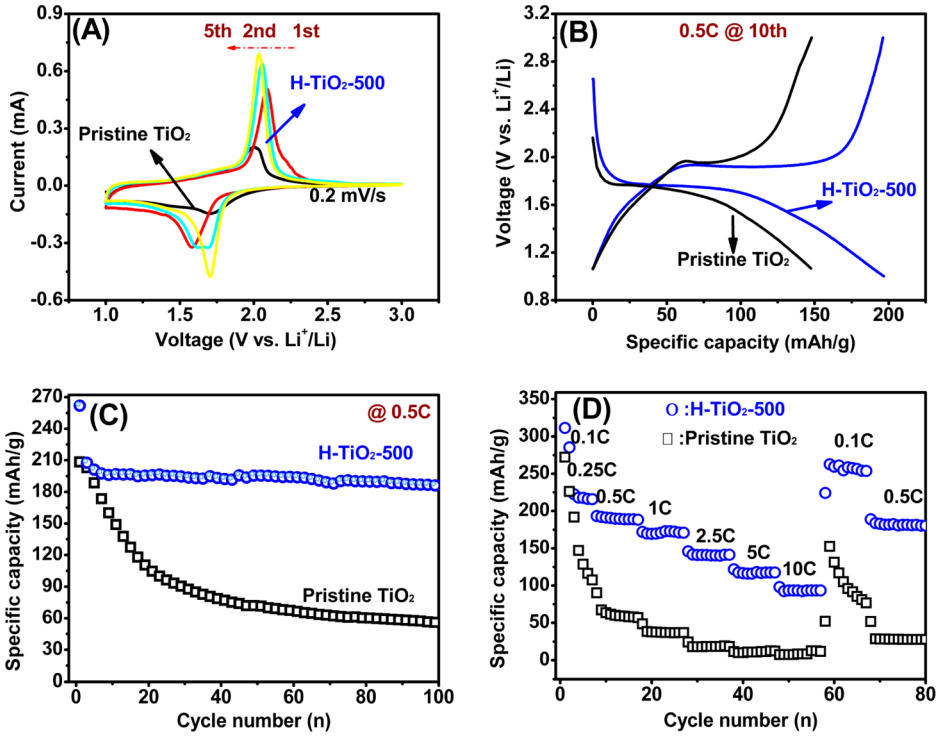

Figure 5. Electrochemical tests of pristine TiO_2 and H-TiO_2-500. (A) CVs at a scan rate of 0.2 mV/s (voltage range of 1.0−3.0 V); (B) galvanostatic charge/discharge voltage profiles at 0.5 C between voltage limits of 1 and 3 V (data taken from the 10th cycle); (C) cycling performance up to 100 cycles at 0.5 C; (D) specific discharge capacity at various C-rates of 0.1, 0.25, 0.5, 1, 2.5, 5, and 10 C. (1 C = 336 mA/g).

positron lifetime, correspondingly. Therefore, the values of τ_2 are much larger than those of τ_1. Meanwhile, the ratio of I_1 to I_2 (I_1/I_2) is used to compare the relative concentration of small-size bulk defects to large-size surface defects. It is also found that the τ_2 of H-TiO_2-500 (385.8 ps) is much longer than that of pristine TiO_2 (357.0 ps), indicating reduced surrounding electron density in the former structure. Moreover, the ratio I_1/I_2 of H-TiO_2-500 is as high as 1.98 more than double of that of pristine TiO_2 (I_1/I_2 = 0.94). Such results clearly demonstrate that some larger-size vacancy clusters are induced into the H-TiO_2-500, which results from interaction between the small neutral Ti^{3+}-oxygen vacancy associates.[33]

The pristine and H-TiO_2-500 samples are used as anode materials to assemble half lithium batteries and undergo a series of electrochemical tests under identical conditions. The CVs (Figure 5A) show dramatic differences between them: a pair of pronounced redox peaks, situated at 1.571/2.095 V, is observed on the first cycle for H-TiO_2-500, which is associated with the insertion/deinsertion processes of Li^+ in the TiO_2 framework, following the redox reaction: $TiO_2 + xLi^+ + xe^- \leftrightarrow Li_xTiO_2$, while a minor reduction and oxidation peak appears on the CV curves for pristine TiO_2. Meanwhile, from the second cycle onward, as shown in Figure 5A, the CV curves for H-TiO_2-500 are pretty reproducible, indicating a good reversibility for the Li^+ intercalation/deintercalation process during cycling.

The galvanostatic discharge/charge curves of the 10th cycle at 0.5 C for pristine TiO_2 and H-TiO_2-500 are illustrated in Figure 5B. Both the TiO_2 materials display typical cathodic and anodic potential plateau characteristic of anatase TiO_2 at ∼1.75 and 1.95 V versus Li/Li^+. However, H-TiO_2-500 has a greatly enhanced discharge specific capacity of 196.1 mAh/g and columbic efficiency of 99.7%, while pristine TiO_2 only achieved 147.5 mAh/g and 95.6% at 0.5 C. As shown in Figure 5C, H-TiO_2-500 demonstrates much more stable cycling performance, and the discharge capacity can be retained at 186 mAh/g after 100 cycles, while only 55.3 mAh/g can be kept after 100 cycles for pristine TiO_2. The improved cycling performance of the blue H-TiO_2-500 can be credited to the decrease in particle sizes, crystalline dislocation, and presence of oxygen vacancy/Ti^{3+} induced by the hydrogenation process.

Figure 5D shows the rate capability of H-TiO_2-500 and pristine TiO_2 with current densities varying from 0.1 C to 10 C. Each of the two samples exhibits high initial discharge capacity at 0.1 C; however, a sharp capacity decay occurs in the following two cycles for the pristine TiO_2, while the H-TiO_2-500 retains dramatically higher discharge capacity. As the increasing the C rate, the pristine TiO_2 undergoes even further decay of the capacities, but the H-TiO_2-500 anode material can endure more radical changes of current density. Even after 60 cycles with successively increasing current densities from 0.1 to 10 C, H-TiO_2-500 can still retain a discharge capacity of ∼100 mAh/g, and when the rate returns to 0.1 C, the discharge capacity reverses to the original value of 275 mAh/g at 0.1 C. These results suggest that the advantages of hydrogenation treatment on TiO_2 in respect of the cyclability are more significant.

Moreover, it can be found that our prepared H-TiO_2-500 shows some advantages in electrochemical capacity under different conditions over typical nanoporous anatase TiO_2 mesocrystals,[7] traditionally hydrogenated blue rutileTiO_2,[15] and anatase $TiO_{2-\delta}$[19] (Figure S4). Such significant improvement on the electrochemical properties can be attributed to the enhanced electronic conductivity as well as Li^+ diffusion by hydrogenation treatment. As shown in Figure S11, the EIS results demonstrate that H-TiO_2-500 has lowest electronic resistance (Rct) and Warburg resistance (W), which can be

DOI: 10.1021/acsami.5b07000
ACS Appl. Mater. Interfaces 2015, 7, 23431−23438

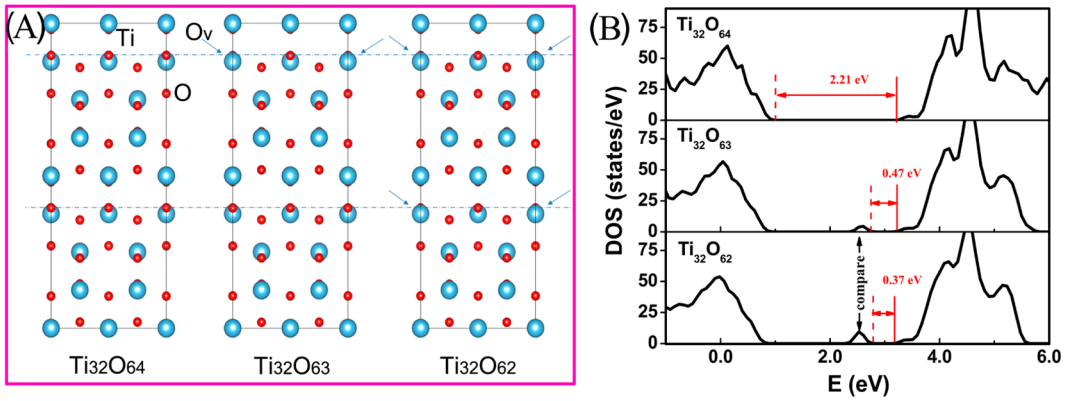

Figure 6. Density functional theory theoretical calculations: (A) Calculated models of $Ti_{32}O_{64}$ (bulk TiO_2), $Ti_{32}O_{63}$ (1.56% oxygen deficiency), and $Ti_{32}O_{62}$ (3.13% oxygen deficiency) (arrow: oxygen vacancy); (B) the total density states for the three TiO_2 models. The red dash lines mean the Fermi level in three difference model.

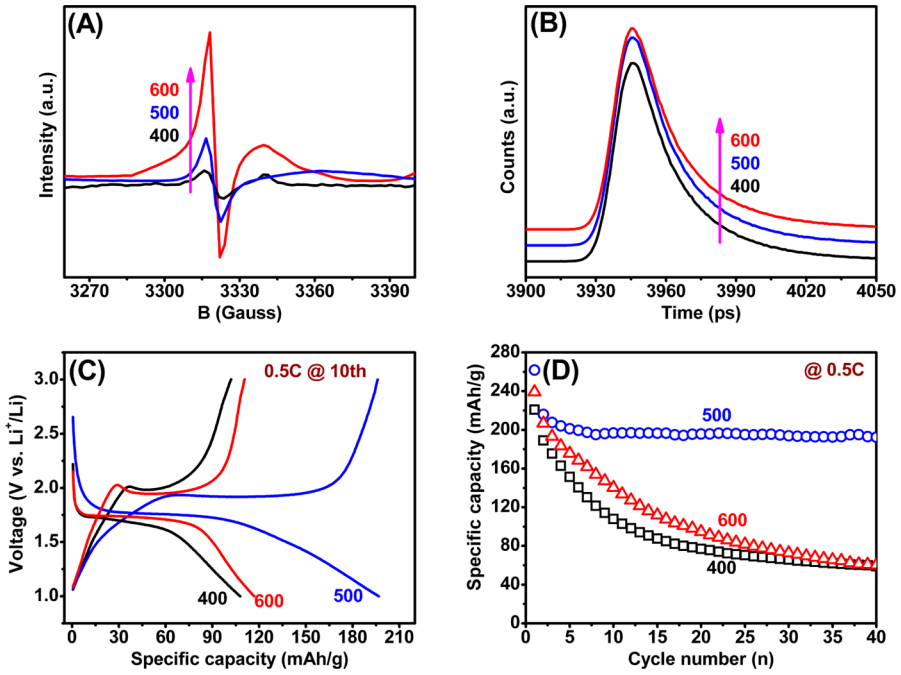

Figure 7. (A) EPR spectra, (B) PALS spectra, (C) galvanostatic charge/discharge profiles (data taken from the 10th cycle), (D) cycling performance up to 100 cycles at 0.5 C of H-TiO_2 prepared at different hydrogenation temperatures.

probably ascribed from abundant oxygen vacancies and Ti^{3+} created by hydrogenation treatment in TiO_2 for improved electrical conductivity and the spitting distance between the oxygen vacancies and the Ti^{3+} cores that could repel the positively charged Li^+ and deliver them into other Ti^{3+} cores to accelerate the Li^+ transport.[35]

Note that the decreased particle size also plays an important role in shortening distance for Li^+ transport and accelerate Li^+ transport. To verify this point, we synthesize an oxygen-vacancy-free TiO_2 (denoted as TiO_2-17 nm-R) with a same size as H-TiO_2-500 via second heat treatment of H-TiO_2-500 under air to remove oxygen vacancy but keep its structure (Figures S5−S7). The cycling performance tests (Figure S8) present that the performance of TiO_2-17 nm-R sample is little higher than pristine TiO_2 but far from H-TiO_2. Therefore, we can conclude that it is the synergistic effect from oxygen vacancy/Ti^{3+} and decreased size that enhances the electronic conductivity as well as Li^+ transport, resulting in a high-capacity and stable TiO_2 material for Li-ion battery.

Furthermore, the mechanism of oxygen-deficiency/Ti^{3+} on the electron conductivity of TiO_2 is studied by DFT calculations. As shown in Figure 6A, three calculation models of large supercell, including $Ti_{32}O_{64}$ (bulk TiO_2), $Ti_{32}O_{63}$ (1.56% oxygen vacancy), and $Ti_{32}O_{62}$ (3.13% oxygen vacancy), are established through removing lattice oxygen between two interstitial voids in the hydrogenation reduction process. The red balls stand for oxygen atom and green for titanium atom; the arrow indicates the missing location of O atom, namely, the location of oxygen-deficiency. Projection of the 2*2*2 TiO_2 supercell is on the ac-plane (the corresponding stereogram is shown in Figure S9). It can be found from the total density of states (DOSs) in Figure 6B that the Fermi level increases from ~1.00 eV for TiO_2 to ~2.76 eV for $Ti_{32}O_{63}$ and 2.79 eV to $Ti_{32}O_{62}$. Moreover, the calculated intrinsic band gap (Eg) for pristine TiO_2 is 2.21 eV, which is in line with previous

DOI: 10.1021/acsami.5b07000
ACS Appl. Mater. Interfaces 2015, 7, 23431−23438

experimental and computational results,[36,37] while the calculated Eg values of $Ti_{32}O_{63}$ and $Ti_{32}O_{62}$ dramatically drop to 0.47 and 0.37 eV, respectively. Therefore, it can be concluded that the electronic conductivity can be enhanced via adjusting the properties of Eg by oxygen vacancies. In addition, comparing the DOSs of $Ti_{32}O_{63}$ and $Ti_{32}O_{62}$, more DOSs are found below Fermi level in $Ti_{32}O_{62}$ than that in $Ti_{32}O_{63}$, suggesting a higher charge carrier concentration with increase of oxygen vacancies. The above results illustrate that the decrease of band gap and the increase of DOSs below Fermi level in the presence of oxygen vacancies might be the two reasons for the improvement of electronic conductivity of the hydrogenated TiO_2.

The effect of hydrogenation temperature on electrochemical properties of H_2-treated TiO_2 is also studied. A series of H_2 treated anatase (XRD in Figure S10) are prepared at different hydrogenation temperatures of 400, 500, and 600 °C. Figure 7A is their low-temperature EPR spectra. The typical peaks at gauss values of ca. 3366 associated with the signals of oxygen vacancies are observed for all the three H_2-treated samples, and the concentration is gradually increased as the hydrogenation temperature is elevated from 400 to 600 °C. In addition, the positron lifetime component τ_2 reduces with increasing the hydrogenation temperature as compared in Table 1, and Figure 7B is the initial graph of matching PALS spectra. The EIS results in Figure S11 and Table S1 demonstrate that the electronic resistance (R_{ct}) of TiO_2 after hydrogenation at 400 or 600 °C is higher than that at 500 °C, suggesting that 500 °C is the optimal condition for the improvement of electronic conductivity. Furthermore, the Warburg resistance (W) is obviously reduced for all hydrogenated TiO_2 samples, indicating that the ionic diffusion process inside electrode is accelerated significantly probably due to the shortened Li-ion transport path resulting from the reduced size under hydrogenation process. The above results reveal that the oxygen vacancies mostly determine the electronic conductivity for hydrogenated TiO_2.

Interestingly, the electrochemical results in Figure 7C,D demonstrate that there is not an obvious trend of linear relationship between the Li-storage performance and the concentration of oxygen vacancies. It can be seen that the specific discharge capacity of H-TiO_2-500 is much higher than that of H-TiO_2-400 and H-TiO_2-600, and the former also exhibits much better cycling performance than the latter two, as shown in Figure 7D. The relationship between the lithium storage properties and the concentration of the oxygen vacancies has been discussed by Shin et.al.[19] who declared that well-balanced Li^+/e^- transport is the key factor for high-performance TiO_2 anode. In their study, the prolonged hydrogenation treatment time results in a greater electronic conductivity but a smaller Li^+ conductivity due to the higher concentration oxygen vacancies. A proper degree of reduction must be desired for high-performance electrode materials. Our results also reveal that in spite of more oxygen vacancies generated at higher hydrogenation temperatures; the Li^+ diffusion is not obviously enhanced due to the depression of free Li^+ concentration by excess electrons. As a consequence, the TiO_2 hydrogenated at 500 °C in this situation has the well-balanced Li^+/e^- transport, resulting in a greatest improvement over Li-storage performance.

CONCLUSION

In summary, blue oxygen vacancies anatase TiO_2 anodes were synthesized using a modified hydrogenation process for LIBs. Systematical characterizations reveal that Ti^{3+}/oxygen vacancy was successfully injected in TiO_2 with a controllable concentration by hydrogenation temperature. Further experiments and theory calculation demonstrate that oxygen vacancies can act on the band gap and then decrease the Eg and increase the DOSs below Fermi level, which facilitate the enhancement of the electronic conductivity of TiO_2. Meanwhile, the spitting distance between the oxygen vacancies and the Ti^{3+} cores could repel the positive charged Li^+ and deliver them into other Ti^{3+} cores to accelerate the Li^+ transport. Further accompanied with the synergetic effect from the reduced sized-derived shortened transport path distance, the H-TiO_2-500 with a well-balanced Li^+/e^- transport possesses a high specific capacity, as well as greatly enhanced cycling stability and rate performance in comparison with the other TiO_2 samples, endowing it as a potential high-performance anode for lithium batteries.

ASSOCIATED CONTENT

Supporting Information

The Supporting Information is available free of charge on the ACS Publications website at DOI: 10.1021/acsami.5b07000.

Relevant XRD, TEM, particle size distributions, original Ti 2p XPS curves, low- and room-temperature EPR, EIS results and additional cycle performance for TiO_2, H-TiO_2 and/or TiO_2-17 nm-R; electrochemical property comparison, and DFT calculation mode. (PDF)

AUTHOR INFORMATION

Corresponding Authors

*E-mail: gbji@nuaa.edu.cn. (G.J.)
*E-mail: chuhong.zhang@scu.edu.cn. (C.Z.)

Author Contributions

J.Z., G.B.J., and Y.S.L. conceived and designed the study; J.Z. performed the experiments, and J.Z., Y.S.L., and G.B.J. analyzed the data; P.Z., X.Z.C., and B.Y.W. provided the PALS test; X.G.Z., Y.Z., and D.N.S. performed the density functional theory (DFT) calculations. J.Z. wrote the paper; J.Z., C.H.Z., and G.B.J. reviewed and edited the manuscript. All authors read and approved the manuscript.

Notes

The authors declare no competing financial interest.

ACKNOWLEDGMENTS

This work was financially supported by the National Natural Science Foundation of China (No. 11575085), National Basic Research Program of China (973 program, No: 2013CB934700), and the Priority Academic Program Development of Jiangsu Higher Education Institutions.

REFERENCES

(1) Shin, J. Y.; Samuelis, D.; Maier, J. Sustained Lithium-Storage Performance of Hierarchical, Nanoporous Anatase TiO_2 at High Rates: Emphasis on Interfacial Storage Phenomena. *Adv. Funct. Mater.* **2011**, *21*, 3464−3472.

(2) Dambournet, D.; Belharouak, I.; Amine, K. Tailored Preparation Methods of TiO_2 Anatase, Rutile, Brookite: Mechanism of Formation and Electrochemical Properties. *Chem. Mater.* **2010**, *22*, 1173−1179.

DOI: 10.1021/acsami.5b07000
ACS Appl. Mater. Interfaces 2015, 7, 23431−23438

(3) Saravanan, K.; Ananthanarayanan, K.; Balaya, P. Mesoporous TiO_2 with High Packing Density for Superior Lithium Storage. *Energy Environ. Sci.* **2010**, *3*, 939−948.
(4) Sun, C. H.; Yang, X. H.; Chen, J. S.; Li, Z.; Lou, X. W.; Li, C. Z.; Smith, S. C.; Lu, G. Q.; Yang, H. G. Higher Charge/discharge Rates of Lithium-ions across Engineered TiO_2 Surfaces Leads to Enhanced Battery Performance. *Chem. Commun.* **2010**, *46*, 6129−6131.
(5) Ortiz, G. F.; Hanzu, I.; Djenizian, T.; Lavela, P.; Tirado, J. L.; Knauth, P. Alternative Li-Ion Battery Electrode Based on Self-Organized Titania Nanotubes. *Chem. Mater.* **2009**, *21*, 63−67.
(6) Liu, S.; Jia, H.; Han, L.; Wang, J.; Gao, P.; Xu, D.; Yang, J.; Che, S. N. Nanosheet-Constructed Porous TiO_2-B for Advanced Lithium Ion Batteries. *Adv. Mater.* **2012**, *24*, 3201−3204.
(7) Ye, J. F.; Liu, W.; Cai, J. G.; Chen, S.; Zhao, X. W.; Zhou, H. H.; Qi, L. M. Nanoporous Anatase TiO_2 Mesocrystals: Additive-Free Synthesis, Remarkable Crystalline-Phase Stability, and Improved Lithium Insertion Behavior. *J. Am. Chem. Soc.* **2011**, *133*, 933−940.
(8) Das, S. K.; Darmakolla, S.; Bhattacharyya, A. J. High Lithium Storage in Micrometre Sized Mesoporous Spherical Self-assembly of Anatase Titania Nanospheres and Carbon. *J. Mater. Chem.* **2010**, *20*, 1600−1606.
(9) Ding, S. J.; Chen, J. S.; Lou, X. W. One Dimensional Hierarchical Structure Composed of Metal Oxide Nanosheets on CNT Backbone and Their Lithium Storage Properties. *Adv. Funct. Mater.* **2011**, *21*, 4120−4125.
(10) Cao, F. F.; Guo, Y. G.; Zheng, S. F.; Wu, X. L.; Jiang, L. Y.; Bi, R. R.; Wan, L. J.; Maier, J. Symbiotic Coaxial Nanocables: Facile Synthesis and an Efficient and Elegant Morphological Solution to the Lithium Storage Problem. *Chem. Mater.* **2010**, *22*, 1908−1914.
(11) Wang, D. H.; Choi, D.; Li, J.; Yang, Z.; Nie, Z.; Kou, R.; Hu, D.; Wang, C.; Saraf, L. V.; Zhang, J.; Aksay, I. A.; Liu, J. Self-Assembled TiO_2-Graphene Hybrid Nanostructures for Enhanced Li-Ion Insertion. *ACS Nano* **2009**, *3*, 907−914.
(12) Ventosa, E.; Mei, B.; Xia, W.; Muhler, M.; Schuhmann, W. TiO_2 (B)/Anatase Composites Synthesized by Spray Drying as High Performance Negative Electrode Material in Li-Ion Batteries. *ChemSusChem* **2013**, *6*, 1312−1315.
(13) Aldon, L.; Kubiak, P.; Picard, A.; Jumas, J. C.; Olivier-Fourcade, J. Size Particle Effects on Lithium Insertion into Sn-doped TiO_2 Anatase. *Chem. Mater.* **2006**, *18*, 1401−1406.
(14) Wan, Z.; Cai, R.; Jiang, S. M.; Shao, Z. P. Nitrogen- and TiN-modified $Li_4Ti_5O_{12}$: One-Step Synthesis and Electrochemical Performance Optimization. *J. Mater. Chem.* **2012**, *22*, 17773−17781.
(15) Qiu, J. X.; Li, S.; Gray, E.; Liu, H. W.; Gu, Q. F.; Sun, C. H.; Lai, C.; Zhao, H. J.; Zhang, S. Q. Hydrogenation Synthesis of Blue TiO_2 for High-Performance Lithium-Ion Batteries. *J. Phys. Chem. C* **2014**, *118*, 8824−8830.
(16) Lu, Z. G.; Yip, C. T.; Wang, L. P.; Huang, H. T.; Zhou, L. M. Hydrogenated TiO_2 Nanotube Arrays as High-Rate Anodes for Lithium-Ion Microbatteries. *ChemPlusChem* **2012**, *77*, 991−1000.
(17) Ventosa, E.; Tymoczko, A.; Xie, K. P.; Xia, W.; Muhler, M.; Schuhmann, W. Low Temperature Hydrogen Reduction of High Surface Area Anatase and Anatase/β-TiO_2 for High-charging-rate Batteries. *ChemSusChem* **2014**, *7*, 2584−2589.
(18) Cronemeyer, D. C. Infrared Absorption of Reduced Rutile Ti Single Crystals. *Phys. Rev.* **1959**, *113*, 1222−1226.
(19) Shin, J. Y.; Joo, J. H.; Samuelis, D.; Maier, J. Oxygen-Deficient $TiO_{2-\delta}$ Nanoparticles via Hydrogen Reduction for High Rate Capability Lithium Batteries. *Chem. Mater.* **2012**, *24*, 543−551.
(20) Sundaramurthy, J.; Aravindan, V.; Kumar, P. S.; Madhavi, S.; Ramakrishna, S. Electrospun $TiO_{2-\delta}$ Nanofibers as Insertion Anode for Li-Ion Battery Applications. *J. Phys. Chem. C* **2014**, *118*, 16776−16781.
(21) Chen, X. B.; Liu, L.; Liu, Z.; Marcus, M. A.; Wang, W. C.; Oyler, N. A.; Grass, M. E.; Mao, B. H.; Glans, P. A.; Yu, P. Y.; Guo, J. H.; Mao, S. S. Properties of Disorder-Engineered Black Titanium Dioxide Nanoparticles through Hydrogenation. *Sci. Rep.* **2013**, *3*, 1−7.
(22) Liu, N.; Schneider, C.; Freitag, D.; Hartmann, M.; Venkatesan, U.; Müller, J.; Spiecker, E.; Schmuki, P. Black TiO_2 Nanotubes: Cocatalyst-Free Open-Circuit Hydrogen Generation. *Nano Lett.* **2014**, *14*, 3309−3313.
(23) Han, X. G.; Kuang, Q.; Jin, M. S.; Xie, Z. X.; Zheng, L. S. Synthesis of Titania Nanosheets with a Large Percentage of Exposed (001) Facets and Related Photocatalytic Properties. *J. Am. Chem. Soc.* **2009**, *131*, 3152−3153.
(24) Kackell, P.; Furthmüller, J.; Bechstedt, F.; Kresse, G.; Hafner, J. Characterization of Carbon-carbon Bonds on the SiC (001) c (2 × 2) Surface. *Phys. Rev. B: Condens. Matter Mater. Phys.* **1996**, *54*, 10304−10307.
(25) Kohn, W.; Sham, L. J. Self-consistent Equations Including Exchange and Correlation Effects. *Phys. Rev.* **1965**, *140*, 1133−1138.
(26) Hammer, B.; Hansen, L. B.; Nørskov, J. K. Improved Adsorption Energetics within Density-functional Theory Using Revised Perdew-Burke-Ernzerhof Functionals. *Phys. Rev. B: Condens. Matter Mater. Phys.* **1999**, *59*, 7413−7421.
(27) Anisimov, V. I.; Zaanen, J.; Andersen, O. K. Band Theory and Mott Insulators: Hubbard U instead of Stoner I. *Phys. Rev. B: Condens. Matter Mater. Phys.* **1991**, *44*, 943−954.
(28) Lisachenko, A. A.; Kuznetsov, V. N.; Zakharov, M. N.; Mikhailov, R. V. The Interaction of O_2, NO, and N_2O with Surface Defects of Dispersed Titanium Dioxide. *Kinet. Catal.* **2004**, *45*, 189−197.
(29) Biesinger, M. C.; Lau, L. W. M.; Gerson, A. R.; Smart, R. S. C. Resolving Surface Chemical States in XPS Analysis of First Row Transition Metals, Oxides and Hydroxides: Sc, Ti, V, Cu and Zn. *Appl. Surf. Sci.* **2010**, *257*, 887−898.
(30) Yamashita, T.; Hayes, P. Analysis of XPS Spectra of Fe^{2+} and Fe^{3+} Ions in Oxide Materials. *Appl. Surf. Sci.* **2008**, *254*, 2441−2449.
(31) Huo, J. C.; Hu, Y. J.; Jiang, H.; Li, C. Z. In Situ Surface Hydrogenation Synthesis of Ti^{3+} Self-doped TiO_2 with Enhanced Visible Light Photoactivity. *Nanoscale* **2014**, *6*, 9078−9084.
(32) Xing, M. Y.; Zhang, J. L.; Chen, F.; Tian, B. Z. An Economic Method to Prepare Vacuum Activated Photocatalysts with High Photo-activities and Photosensitivities. *Chem. Commun.* **2011**, *47*, 4947−4949.
(33) Jiang, X. D.; Zhang, Y. P.; Jiang, J.; Rong, Y. S.; Wang, Y. C.; Wu, Y. C.; Pan, C. X. Characterization of Oxygen Vacancy Associates within Hydrogenated TiO_2: a Positron Annihilation Study. *J. Phys. Chem. C* **2012**, *116*, 22619−22624.
(34) Kong, M.; Li, Y.; Chen, X.; Tian, T.; Fang, P.; Zheng, F.; Zhao, X. Tuning the Relative Concentration Ratio of Bulk Defects to Surface Defects in TiO_2 Nanocrystals Leads to High Photocatalytic Efficiency. *J. Am. Chem. Soc.* **2011**, *133*, 16414−16417.
(35) Ma, Y.; Ji, G.; Ding, B.; Lee, J. Y. Facile Solvothermal Synthesis of Anatase TiO_2 Microspheres with Adjustable Mesoporosity for the Reversible Storage of Lithium Ions. *J. Mater. Chem.* **2012**, *22*, 24380−24385.
(36) Yang, K. S.; Dai, Y.; Huang, B. B.; Whangbo, M. H. Density Functional Characterization of the Band Edges, the Band Gap States, and the Preferred Doping Sites of Halogen-Doped TiO_2. *Chem. Mater.* **2008**, *20*, 6528−6534.
(37) Nagaveni, K.; Hegde, M. S.; Ravishankar, N.; Subbanna, G. N.; Madras, G. Synthesis and Structure of Nanocrystalline TiO_2 with Lower Band Gap Showing High Photocatalytic Activity. *Langmuir* **2004**, *20*, 2900−2907.

DOI: 10.1021/acsami.5b07000
ACS Appl. Mater. Interfaces 2015, 7, 23431−23438